7

THE METHOD OF CONFORMING BOUNDARY ELEMENTS FOR TRANSIENT ELECTROMAGNETICS

A. C. Cangellaris and K. K. Mei

7.1 Introduction

Traditionally, electromagnetic wave scattering computations are done in the frequency domain. Recently, however, there has been an increasing interest in the solution of transient electromagnetic scattering, which is prompted by a number of reasons. Current development in wideband radar design for higher resolution has created interest in the investigation of the impulse response of conducting bodies for target identification purposes. The electromagnetic pulse (EMP) problem is another area of great interest which is, essentially, a transient problem. Nonlinear scattering and radiation problems, which have become of great interest in recent years, are, in general, more easily addressed by obtaining the transient solution directly. The ability to compute accurately the transient electromagnetic fields in the presence of dispersive media is of great importance in remote sensing methods for de-

termining the electromagnetic parameters of inaccessible regions. The simplicity with which the time-dependent form of Maxwell's equations can be integrated in the presence of composite structures with different electric and magnetic properties suggests the possibility for a transient analysis of integrated dielectric waveguides and other components for microwave and millimeter-wave integrated circuits.

The time-dependent integral equation formulation, first reported by Bennett and Weeks [1], has dominated the numerical solution of transient electromagnetic scattering over the past years [2–4]. More recently, iterative methods have been introduced in the solution of the above integral equations [5,6], as an alternative to the marching-on-in-time procedure which was found to lead to rapid growth of spurious oscillations [7] due to the accumulation of numerical error. The new generation of computers, with the vast memory capacities and the parallel processing architecture that favors simple sequential operations, has opened new possibilities for the direct time-domain solution of electromagnetic problems. A very interesting finite-difference scheme was first presented by Yee [8] . Its simplicity and efficiency attracted many investigators and the method found many applications [9–14] (also see Chapter 8 of this book). A severe limitation of this formulation was the use of square or cubic cells to approximate the geometry of the scatterer. These cells introduce important boundary distortion in the problem which affects the satisfaction of the related electromagnetic boundary conditions on conducting surfaces and/or dielectric interfaces. The hope for a more flexible method led to the use of the conformal finite-differences [15] and later on to the point-matched finite-elements, the conforming boundary elements, as well as other finite-elements formulations of the problem [16]. The point-matched finite elements were used to study transient electromagnetic scattering from buried objects [17], while an introduction to the method of conforming boundary elements was presented in a recent paper by Cangellaris, et al. [18]. Two additional modified time-domain finite-difference schemes for use with nonrectangular structures have been reported recently [19,20].

In this paper, the method of conforming boundary elements is reviewed and extended to geometries with corners and wedges. Furthermore, the various errors introduced by the numerical discretization are examined in detail. The importance of the artificial boundary that truncates the computational domain, as well as its impact on the numerical solution is also discussed. Numerical examples in two and three dimensions are presented, along with comparisons with available ex-

perimental results. These examples demonstrate the efficiency of the method and its versatility in dealing with large, composite structures of arbitrary shape.

7.2 Initial Boundary Value Problem

The general problem this paper is dealing with is the interaction of an electromagnetic wave with perfectly conducting and/or dielectric obstacles in free space. No restriction is imposed on the dielectric permittivity of the structure, which can have any desired spatial variation $\epsilon(\bar{r})$. We must mention that losses in the dielectrics can be accounted for by introducing a finite conductivity $\sigma(\bar{r})$. Since linearity is assumed, one can decompose the total field into incident and scattered fields. The incident field $\overline{E}^{in}$ is defined to be the field that would exist in the absence of the scatterers. If $\overline{E}^{tot}$ denotes the total field, then the scattered field is defined as

$$\overline{E}^{sc} = \overline{E}^{tot} - \overline{E}^{in} \tag{1}$$

In a source-free region the macroscopic electromagnetic phenomena are governed by Maxwell's equations

$$\nabla \times \overline{E}^{tot}(\bar{r},t) = -\mu_0 \frac{\partial \overline{H}^{tot}}{\partial t} \tag{2a}$$

$$\nabla \times \overline{H}^{tot}(\bar{r},t) = \epsilon(\bar{r}) \frac{\partial \overline{E}^{tot}}{\partial t} + \sigma(\bar{r}) \overline{E}^{tot} \tag{2b}$$

For a well-posed initial boundary value problem, the uniqueness theorem for Maxwell's equations [21] requires that

(a) $\overline{E}(\bar{r}, t = 0)$ and $\overline{H}(\bar{r}, t = 0)$ must be known everywhere inside the domain of interest. Notice that if the *known* incident field is not allowed to reach the scatterer before $t = 0$, then the initial condition for the unknown scattered fields is

$$\overline{E}^{sc}(\bar{r}, t = 0) = \overline{H}^{sc}(\bar{r}, t = 0) = 0 \tag{3}$$

(b) The tangential component of $\overline{E}^{tot}$ or $\overline{H}^{tot}$ on the boundaries of the domain of interest must be known for all $t \geq 0$.

For the case of a perfect conductor, its surface is part of the boundary, and on it

$$\hat{n} \times \overline{E}^{tot}(t) = 0 \tag{4}$$

where $\hat{n}$ is the unit normal vector on the surface. For the boundary at infinity, Sommerfeld's radiation condition [22] must hold; that is, the *scattered* fields must be of an outward travelling wave type. Since the numerical technique under consideration can treat only a finite computational domain, an artificial boundary is introduced and an equivalent radiation condition is imposed on this truncation boundary. The validity of such an approximation is of great importance and is discussed in section 7.3. Finally, we must mention that for the boundary between two regions (i) and (j) with different dielectric and conducting characteristics, the following conditions must be satisfied for all t

$$\hat{n} \times \overline{E}_{(i)}{}^{tot} = \hat{n} \times \overline{E}_{(j)}{}^{tot} \tag{5a}$$

$$\hat{n} \cdot \left(\epsilon_{(i)} \frac{\partial \overline{E}^{tot}_{(i)}}{\partial t} + \sigma_{(i)} \overline{E}^{tot}_{(i)} \right) = \hat{n} \cdot \left(\epsilon_{(j)} \frac{\partial \overline{E}^{tot}_{(j)}}{\partial t} + \sigma_{(j)} \overline{E}^{tot}_{(j)} \right) \tag{5b}$$

where $\hat{n}$ is the unit normal vector on the interface. In what follows, we restrict ourselves to lossless media and we drop the conduction current term in (2b) and (5b). The details for the treatment of lossy media can be found in [17].

7.3 Method of Conforming Boundary Elements

A detailed, tutorial presentation of the point-matched time-domain finite-element method and its special case of the conforming boundary elements can be found in [18]. Here we shall present a summary of the method and its advantages, accompanied by a more detailed discussion of some of the discretization issues that were considered rather briefly in [18].

The computational domain which is truncated by means of an artificial radiation boundary is discretized as shown in Fig. 1. This layout results into two complementary meshes, one for the electric and one for the magnetic field, positioned in such a way that an element of each of the meshes encloses a node of the other. We assume that $\overline{E}$ and $\overline{H}$ can be written in the general functional forms

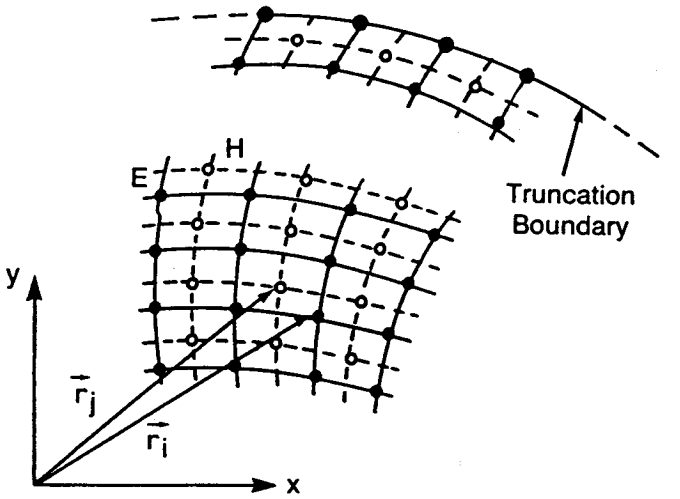

Figure 1 Finite-element discretization of computational domain.

$$\overline{E}(\overline{r},t) \approx \sum_{i=1}^{M} \phi_i(\overline{r})\overline{E}_i(t) \tag{6a}$$

$$\overline{H}(\overline{r},t) \approx \sum_{j=1}^{M} \psi_j(\overline{r})\overline{H}_j(t) \tag{6b}$$

where $\overline{E}_i$'s and $\overline{H}_j$'s are the nodal values of the electric and magnetic fields, respectively, and ϕ_i's and ψ_j's are known basis functions which allow us to describe any desirable variation of the fields within the elements. By an appropriate definition of these functions we can make the field within an element be dependent only on its values at the nodes of the element [18]. Then one can show that a point-matching (collocation) procedure reduces (2*a*, 2*b*) to the following system of state equations

$$\frac{d\overline{H}_j}{dt} = -\frac{1}{\mu_0}\sum_{l=1}^{L}\left(\nabla\phi_l(\overline{r})\right)_{\overline{r}=\overline{r}_j} \times \overline{E}_l(t), \qquad j = 1,2,\ldots,N \tag{7a}$$

$$\frac{d\overline{E}_i}{dt} = \frac{1}{\epsilon(\overline{r}_i)}\sum_{l=1}^{L}\left(\nabla\psi_l(\overline{r})\right)_{\overline{r}=\overline{r}_i} \times \overline{H}_l(t), \qquad i = 1,2,\ldots,M \tag{7b}$$

where, N is the number of magnetic nodes, M is the number of electric nodes, and L is the number of nodes of a single element. For the two-dimensional quadrilateral $L = 4$, while for the three-dimensional hexahedron $L = 8$. The above system of state equations must now be integrated in time. For this purpose, the "leap-frog" method is used [23] (a basic discussion appears in Chapter 1). According to this method, the electric and magnetic fields are discretized in time with time step (δt), with the temporal nodes of $\overline{H}$ between those of $\overline{E}$. Using the simplified notation

$$\overline{E}^n = \overline{E}[t = n(\delta t)] \tag{8a}$$

$$\overline{H}^{n+\frac{1}{2}} = \overline{H}[t = (n + \frac{1}{2})(\delta t)], \qquad n = 0, 1, \ldots \tag{8b}$$

we approximate the time derivatives in (7) by the central difference formulas

$$\left(\frac{d\overline{H}_j}{dt}\right)_{n(\delta t)} \approx \frac{\overline{H}_j^{n+\frac{1}{2}} - \overline{H}_j^{n-\frac{1}{2}}}{\delta t} \tag{9a}$$

$$\left(\frac{d\overline{E}_i}{dt}\right)_{(n+\frac{1}{2})(\delta t)} \approx \frac{\overline{E}_i^{n+1} - \overline{E}_i^{n}}{\delta t} \tag{9b}$$

Substituting (9a,b) in (7a,b) and rearranging we obtain the following explicit recurrence formulas

$$\overline{H}_j^{n+\frac{1}{2}} = \overline{H}_j^{n-\frac{1}{2}} - \frac{(\delta t)}{\mu_0} \sum_{l=1}^{L} \left(\nabla \phi_l(\overline{r})\right)_{\overline{r}=\overline{r}_j} \times \overline{E}_l^n, \qquad j = 1, 2, \ldots, N \tag{10a}$$

$$\overline{E}_i^{n+1} = \overline{E}_i^n + \frac{(\delta t)}{\epsilon(\overline{r}_i)} \sum_{l=1}^{L} \left(\nabla \psi_l(\overline{r})\right)_{\overline{r}=\overline{r}_i} \times \overline{H}_l^{n+\frac{1}{2}}, \qquad i = 1, 2, \ldots, M \tag{10b}$$

Once the initial conditions at $t = 0$ are known, (10a,b) can be used alternatively to update $\overline{H}_j$'s and $\overline{E}_i$'s at $n = 1, 2, \ldots$.

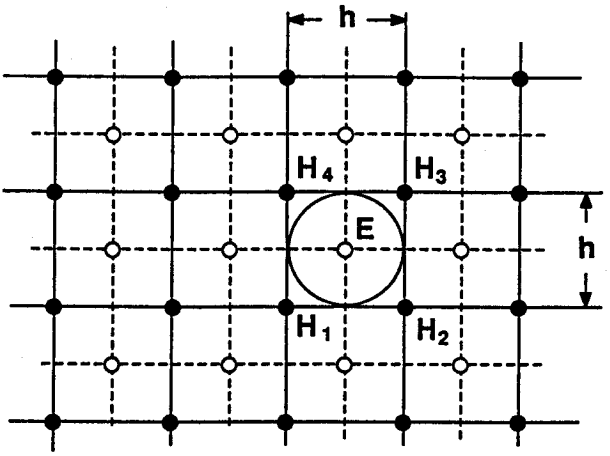

Figure 2 Characteristic circle for the leap-frog scheme.

The method of conforming boundary elements is a special case of the previously discussed point-matched finite-element method. The basic idea behind it is to relax the memory requirements for the storage of coordinates of all the nodes of the finite element mesh by limiting the irregularly shaped elements to the boundary of the scatterer only. In this aspect, this method can be considered as a technique which puts together the advantages of both the finite-element and the finite-difference methods. That is, the few irregularly shaped boundary elements conform the geometry of interest, while the regularity of the rest of the grid is conserved to take advantage of the attractive feature of the finite-difference method where the index numbers of each node contain the nodal coordinates. It is also known that the leap-frog integration of (10a,b) is stable under the condition [23]

$$c(\delta t) \leq h \tag{11}$$

where c is the velocity of propagation in the medium. Notice that with this scheme the Courant limit can be reached in all cases regardless of the number of dimensions of the problem. This can be demonstrated easily by viewing the leap-frog scheme proposed above as a two-step integration of the time-dependent wave equation. Then, the theory of characteristics states that the numerical scheme is stable, if, and only if, the domain of dependence for the discrete equation includes that for the differential equation. For the two-dimensional case considering the electric node E in Fig. 2, the domain of dependence for the discrete

equation that updates the value of this node by half a time step is the square $H_1H_2H_3H_4$. On the other hand, the characteristics for the wave equation in two dimensions are the conical surfaces

$$(x - x_0)^2 + (y - y_0)^2 = (ct)^2 \tag{12}$$

with apex at the node under consideration. If we take as the time origin the plane (ct_0) on which the magnetic nodes H_1, H_2, H_3, H_4 have been updated, then the characteristic through E cuts on this plane the circle

$$(x - x_0)^2 + (y - y_0)^2 = \left(c\frac{\delta t}{2}\right)^2 \tag{13}$$

as the domain of dependence for the wave equation. Then, it is easily seen that for stability (11) must hold. The above reasoning can be extended to the study of the stability condition on irregular grids. However, one needs to check, one by one, all the irregular elements in order to derive the stability condition that must be satisfied over the entire mesh. Equation (11) suggests that h should be kept uniform throughout the finite-element mesh in order to avoid limiting the time step to unrealistically small values. Obviously, the method of conforming boundary elements has control of the size of the smallest element while the various automatic mesh generation techniques leave that to chance or, at least, must introduce additional sophisticated restrictions in order to redistribute the nodes for better uniformity [24]. As far as the interpolation functions are concerned, notice that the ∇ operation in $(10a, b)$ restricts us to choose element functions with continuous first derivatives inside the elements. For our purposes the isoparametric quadrilateral elements with the associated bilinear interpolation functions are chosen for 2-D geometries [25], while hexahedron isoparametric elements constitute a natural extension to three dimensions [26]. One can easily check [27] that with this type of elements the numerical scheme of $(10a, b)$ is consistent, and also that positioning of the nodes at the center of gravity of the element ensures the second order accuracy of the numerical approximation. This, in turn, brings us to some necessary discussion related to the conforming elements themselves. In order to keep (11) valid all over the computational domain, we try to use conforming boundary elements that are large enough to *contain* a regular element. However, the selection of these elements should be such that very large elements will also be excluded. As an example for the selection procedure, consider the element $(B_3E_5E_9B_4)$

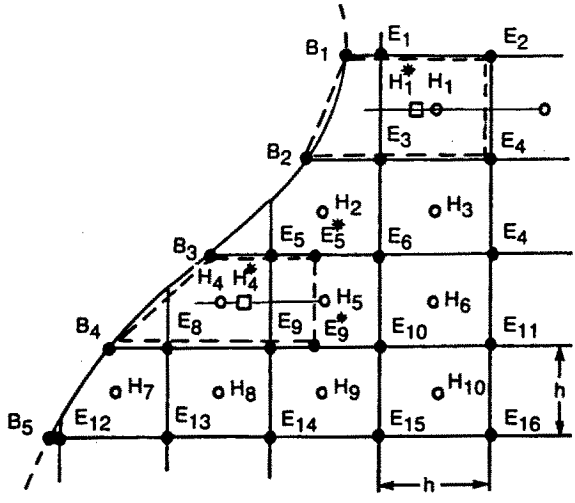

Figure 3 Conforming boundary elements.

of Fig. 3. Obviously, it is not large enough for our purposes, while at the same time the element $(B_3E_6E_{10}B_4)$ is too large. An additional element is then introduced, identified with the dashed line in Fig. 3, where the points E_5^* and E_9^* are such that the length of the segment $(B_3E_5^*)$ equals h. Of course, the electric field at the new nodes E_5^* and E_9^* is determined by interpolation. Since the original node H_4 no longer coincides with the center of gravity of the electric element, an additional magnetic node H_4^* is positioned at the center of gravity of the new element and the value of the original magnetic node (if needed) is computed by extrapolation as in the element under consideration, or by interpolation as in the element $(B_1E_2E_4B_2)$ of the same figure. For smooth, well-resolved geometries, one rarely encounters elements where such an extrapolation procedure is needed. Hence, the departure from the second-order accuracy of the solution due to the first-order accurate extrapolation is very localized and does not affect the overall accuracy and the stability of the numerical integration. There are also some electric nodes that are computed by interpolation, for example, E_{12}, E_8, E_5, E_3, E_1 in Fig. 3.

Finally, we must mention that the boundary condition (4) defines only the tangential component of the electric field for those electric nodes that lie on the conducting surface. Therefore, the continuity equation on the conducting surface

$$\nabla \cdot \overline{J} + \frac{\partial \rho}{\partial t} = 0 \tag{14}$$

is implemented for the computation of the normal component of the electric field. Using the relations

$$\overline{J} = \hat{n} \times \overline{H}^{tot} \tag{15a}$$

$$\rho = \hat{n} \cdot \overline{D}^{tot} \tag{15b}$$

in (14), we get

$$\nabla_0 \cdot (\hat{n} \times \overline{H}^{tot}) = -\hat{n} \cdot \frac{\partial \overline{D}^{tot}}{\partial t} \tag{16}$$

where $\nabla_0 \cdot$ is the surface divergence, involving derivatives along the surface of the body only, and $\hat{n}$ is the unit normal on the surface. The details about the numerical implementation of (16) for the case of conforming boundary elements can be found in [18]. In the same paper, a simple technique for treating interfaces between two media with different dielectric constants was introduced. It is well-known that at such dielectric interfaces the field components or their derivatives are discontinuous. Therefore the interpolation functions over elements that include the interface must be modified to include the appropriate discontinuity. Instead of constructing the appropriate interpolation function (a process that is rather complicated in 2-D and 3-D), fictitious nodes are introduced on either side of the interface which allow us to compute the correct spatial derivatives of the fields using central differences. The values of these fictitious nodes are found rigorously by using the boundary conditions at the interface. For more details on the method, the reader is referred to [18].

Before leaving this section, we would like to point out that *noise* is introduced by the numerical processing. This numerical noise affects the high frequency information. This noise is due to the dispersion introduced by the numerical discretization of the hyperbolic system of Maxwell's curl equations. This dispersion effect results in a *phase error*, the magnitude of which increases with frequency [28, 29] and results in a loss of accuracy. In other words, an initial signal that is not monochromatic will change form as it propagates. Spurious oscillations contaminate the results, particularly when the initial data is in

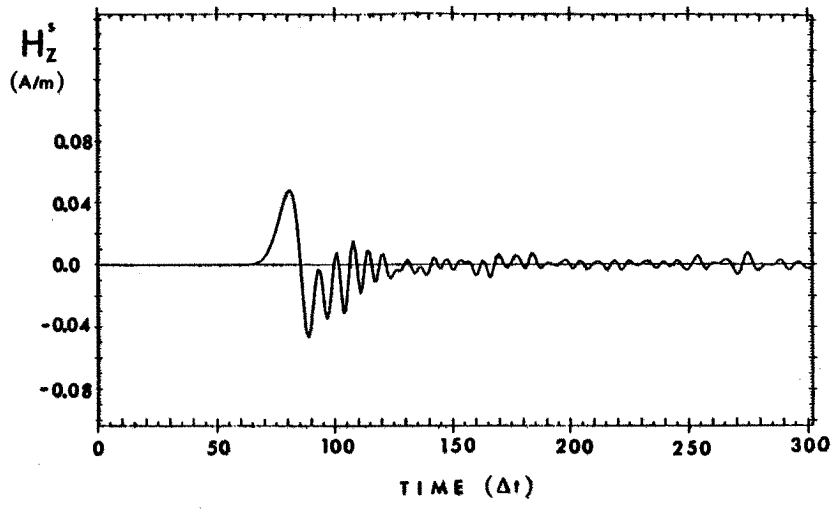

Figure 4 Spurious oscillations due to discontinuity in the initial data.

the form of a sharp signal. These oscillations are demonstrated in Fig. 4 where the back-scattered field from an infinite conducting circular cylinder is presented under the excitation of one half of a Gaussian pulse, that is, a pulse terminated abruptly at its peak value. Another type of numerical error that occurs in the discretization of hyperbolic equations on two- and three-dimensional grids is due to the numerical anisotropy of the velocity of propagation [29]. That is, the velocity of propagation of numerical sinusoidal solutions, in addition to being dependent upon frequency, is also dependent upon direction of propagation. This numerical anisotropy depends on the scheme used for the space discretization. The expression for the numerical phase velocity in terms of the size of the mesh, the frequency of interest, and the direction of propagation can be found by considering the sinusoidal numerical solution to the discretized hyperbolic system. One can show [27] that for the leap-frog scheme of (10a,b) on a regular two-dimensional square grid of size h the numerical phase velocity for a sinusoidal wave of angular frequency ω and with its propagation vector at an angle α with respect to the x-axis is

$$c^* = c\left\{\left[\cos\alpha\frac{\sin(0.5\omega h\cos\alpha)}{0.5\omega h\cos\alpha}\cos(0.5\omega h\sin\alpha)\right]^2\right. \tag{17}$$
$$\left.+\left[\sin\alpha\frac{\sin(0.5\omega h\sin\alpha)}{0.5\omega h\sin\alpha}\cos(0.5\omega h\cos\alpha)\right]^2\right\}^{\frac{1}{2}}$$

where c is the velocity of propagation in the medium. Notice that for a well-resolved wave $\omega h \to 0$ and $c^* \to c$. From (17), one can easily check that the numerical anisotropy is less than 4% for wavelengths longer than $8h$. This sets an upper limit on the highest frequency in the spectrum of the propagating pulses or, translated into the time domain, sets a lower limit on the rise and fall times of the pulses.

Another issue of importance in the numerical discretization is the ratio of the size of the scatterer to the effective width of the exciting pulse. It is well-known that the scattering parameters of a structure can be described in terms of its poles in the complex frequency domain. The number of the poles is determined by the effective maximum frequency of the exciting pulse, which in turn is determined by the spatial width of the pulse. Therefore, for accurate information on the nature of the target, one should decrease the pulse width. This, of course, results in larger number of spatial and temporal samples and consequently, larger storage requirements and longer computational time. There is, therefore, a tradeoff between accurate high-frequency information and cost of computation.

Finally, another source of error in the numerical solution is the numerical condition used at the artificial boundary that truncates the computational domain, and is discussed in the next section.

7.4 Radiation Boundary Condition

The general problem of transient electromagnetic scattering or radiation requires the solution of Maxwell's partial differential equations on an infinite domain. However, for computational expediency, one has to operate within a bounded domain. An artificial boundary is then constructed and appropriate conditions are sought on this boundary in order to simulate an infinite domain. It is desirable that no *reflections* occur from this artificial boundary back into the domain of interest.

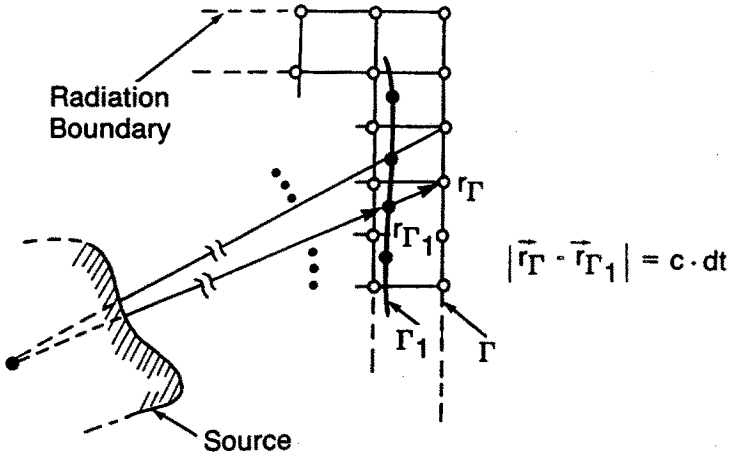

Figure 5 Computation of the scattered field on the radiation boundary.

This is not possible in general, and special restrictions are imposed in order to minimize these reflections. There is a large amount of literature devoted to this subject [30–33]. An exact termination method implements Huygen's principle but is expensive both in storage and computation [33]. From a computational point of view an attractive absorbing boundary condition is one that involves only local spatial and time derivative operations consistent with the simple algorithm of the finite difference or finite element method.

As shown in Fig. 5, a numerical surface Γ is introduced in order to truncate the computational domain. The scheme adopted here for the numerical computation of the fields on Γ is based on the fact that, outside a surface enclosing all the sources of radiation, one can always represent the solution of the scalar wave equation in the following form [34]

$$u(t,r,\theta,\phi) = \sum_{i=1}^{\infty} \frac{f_i\left(t-\frac{r}{c},\theta,\phi\right)}{r^i} \tag{18}$$

where r,θ,ϕ are spherical coordinates and c is the velocity of propagation. Moreover, f_i's can be uniquely determined if the radiation field f_1 at infinity is known. The result in (18) is for the scalar wave equation in three dimensions. For the two-dimensional case, one finds [17] an equivalent expansion

$$u(t,\rho,\phi) = \sum_{i=0}^{\infty} \frac{f_i\left(t-\frac{\rho}{c},\phi\right)}{\rho^{i+\frac{1}{2}}} \tag{19}$$

where ρ, ϕ are polar coordinates. Bayliss and Turkel [40] proposed a family of differential operators B_m constructed in such a way that the m^{th} operator will annihilate the first m terms in the above expansions. In other words, application of the differential operator of order m is equivalent to enforcing the field continuity of the inner solution with the m leading terms of the above expansions on the surface Γ. The higher the order of the operator the more terms are included, and the truncation boundary can be brought closer to the scatterer. As a matter of fact, the use of a second-order radiation boundary condition for Maxwell's equations proposed by Mur [32] has permitted time-domain finite-difference studies of very large targets implementing grids that are truncated within only one or two wavelengths from the target [14] (also see Chapter 8 in this book). Here, we summarize the results for a simple first-order radiation boundary condition that was found to be very efficient from a computational point of view, and we discuss its limitations and the numerical errors associated with it.

If we assume that the surface Γ is far away from the scatterer so that the radiation field will dominate, it is expected that the use of the first term in the above expansions (18,19) will be sufficient to express the behavior of the radiation field there. Hence, we can approximately write

$$u(t,r,\theta,\phi) \approx \frac{1}{r} f_1\left(t-\frac{r}{c},\theta,\phi\right) \tag{20}$$

$$u(t,\rho,\phi) \approx \frac{1}{\sqrt{\rho}} f_0\left(t-\frac{\rho}{c},\phi\right) \tag{21}$$

and the value of the field on Γ can be extrapolated from the knowledge of the field at a point on Γ_1 (Fig. 5)

$$u(t,r_\Gamma,\theta,\phi) \approx \frac{r_{\Gamma_1}}{r_\Gamma} u\left(t-\frac{r_\Gamma - r_{\Gamma_1}}{c},\theta,\phi\right) \tag{22}$$

$$u(t,\rho_\Gamma,\phi) \approx \left(\frac{\rho_{\Gamma_1}}{\rho_\Gamma}\right)^{\frac{1}{2}} u\left(t-\frac{\rho_\Gamma - \rho_{\Gamma_1}}{c},\phi\right) \tag{23}$$

In order to simplify further the numerical implementation of the radiation condition, a convenient choice for the interior point ρ_{Γ_1} would be

$$\rho_\Gamma = \rho_{\Gamma_1} + c(\delta t) \tag{24}$$

where δt is the time step in the numerical integration. The boundary value at ρ_Γ can then be updated directly from the value of the field at ρ_{Γ_1} at the previous time step.

The above analysis can be applied directly to those field components that satisfy the scalar wave equation, i.e., those components that behave like potentials. For two-dimensional problems, this is the case for the E_z component in the TM-case and the H_z component in the TE-case. As far as the three-dimensional case is concerned, one can easily show that the quantity (rE_r) satisfies the scalar wave equation in spherical coordinates [35]. Then according to (20), on the radiation boundary we have

$$E_r(t,r,\theta,\phi) \approx \frac{1}{r^2} f_r\left(t - \frac{r}{c}, \theta, \phi\right) \tag{25}$$

On the other hand, E_θ and E_ϕ do not satisfy the wave equation in spherical coordinates and a radiation condition for them is not that obvious. However, starting with Maxwell's curl equations in spherical coordinates and assuming that the r^{-2} dependence of E_r and H_r makes them negligible compared to (rE_ϕ), (rE_θ) and (rH_ϕ), (rH_θ) in the far-field region, one can show [27] that (rE_ϕ) and (rE_θ) satisfy approximately the one-dimensional wave equation. Therefore, we can write

$$rE_\phi \approx f_\phi\left(t - \frac{r}{c}, \theta, \phi\right) \tag{26}$$

$$rE_\theta \approx f_\theta\left(t - \frac{r}{c}, \theta, \phi\right) \tag{27}$$

Equations (25), (26), and (27) constitute a set of first-order radiation conditions for the artificial boundary in three dimensions.

From the previous discussion, it becomes apparent that the radiation boundary condition imposed on the truncating boundary is an approximate one. Actually, in order to make the numerical implementation of the radiation condition as simple as possible, we assumed

the far-field behavior of the solution in the vicinity of the absorbing boundary. We expect then our solution to be reasonably accurate only if the radiation boundary is indeed in the far-field region for our specific problem. As stated earlier, a choice of a second-order radiation condition would allow us to position the truncation boundary closer to the scatterer; however, its numerical implementation on the finite-element grid was found to be rather involved compared to the adopted first-order scheme. In frequency domain, the far-field region (defined by $r > r_{far}$) for a scatterer with maximum linear dimension d_{max}, is given by Fraunhofer's estimate [36]

$$r_{far} \geq 2\frac{d_{max}^2}{\lambda} \tag{28}$$

where λ is the wavelength of the excitation. This is a frequency dependent relation which states that the radiation boundary must be positioned further and further away from the scatterer as the frequency increases. In other words, for a non-monochromatic signal, as is the case of a general time-varying excitation, a fixed radiation boundary will behave differently for the different frequencies of its spectrum. More specifically, the reflection will be stronger for the higher frequencies. It seems, therefore, that for best results condition (28) must be applied for the smallest wavelength in the pulse spectrum. As we discussed earlier, the minimum effective wavelength on a specific grid with space increment h is $\lambda_{min} \approx 8h$. Therefore, for pulse excitation (28) should be used with $\lambda = 8h$, unless it is known that the power spectrum of the incident pulse is negligible above some frequency f_b such that $\lambda_b = c/f_b > \lambda_{min}$. In that case, (28) should be used with $\lambda = \lambda_b$.

It is interesting to observe that since the numerical phase velocity c^* is dependent on frequency and direction of propagation, it would be more accurate to use c^* instead of c in the radiation condition. Actually, the error we make by assuming that the numerical velocity of propagation is c instead of c^*, could be expressed by using the concept of a *reflection coefficient* $\rho(\alpha,\omega)$

$$\rho(\alpha,\omega) = \frac{c - c^*}{c + c^*} \tag{29}$$

From (17) and (29), we see that such a reflection coefficient is dependent on both frequency and direction of propagation. Furthermore,

(29) makes apparent the fact that significant reflection occurs for wavelengths less than $8h$. Notice that this is a direct consequence of the numerical discretization of the hyperbolic system and reflections at such wavelengths will be present regardless of how far away from the structure we position the artificial boundary.

Another important aspect is the effect of the radiation boundary condition on the overall stability of the numerical computation. A vast amount of theoretical work has been dedicated to the stability of the numerical approximation of hyperbolic equations coupled with boundary conditions on single or multiple artificial boundaries [37–39]. Usually, the instabilities that are due to the presence of the artificial boundary appear as oscillating modes that support the propagation of the *reflected* waves from the artificial boundary back to the computational domain. A study of such modes can be done by examining the numerical group velocity of the solution of Maxwell's equations. Using the numerical phase velocity c^*, as expressed by (17), the group velocity can be found from the relation

$$v_g = \frac{d(\omega c^*(\omega))}{d\omega} \tag{30}$$

One can then show [27] that the numerical group velocity becomes negative for wavelengths shorter than $4h$. This tells us that reflections from the artificial boundary will propagate back to the computational domain as high frequency noise. Unfortunately, these spurious oscillations cannot always be suppressed. Nevertheless, they have been found not to cause any instability in agreement with theoretical predictions based on energy methods [40].

7.5 Field Singularities at Wedges and Corners

When Maxwell's equations are solved in the vicinity of a conducting wedge, singularities in some of the field components or in their spatial derivatives will be present. Then, it is very important to know the manner in which these singular components become infinite for the numerical evaluation of the fields. This knowledge allows us to incorporate the singularity in the numerical algorithm in order to increase its speed of convergence. In our study of the singular field behavior, it is sufficient to consider only distances which are small with respect to the wavelength of interest. As discussed in section 7.2, the effective wavelengths on the grid are limited to $\lambda_{min} \simeq 8h$, hence, it is

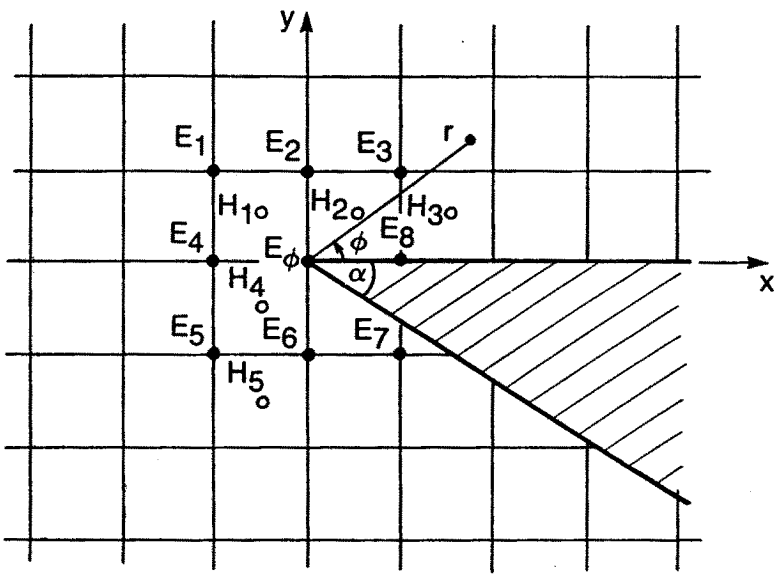

Figure 6 The grid around a conducting wedge.

reasonable to restrict the distances to be no longer than $2h$.

It is well-known that Meixner's condition must be used in the vicinity of a conducting wedge in order to have a unique solution for the specific boundary value problem [35]. Meixner's condition states that the electromagnetic energy density must be integrable over any finite domain even if the domain contains singularities of the fields. We must mention here that according to our definition for the scattered fields, the singularities which do occur are in the scattered field components and not in the incident field.

Let us consider first the TM-case, where the electric field has only one component along the direction of the axis of the wedge (see Fig. 6). One can show [35] that the behavior of the fields at the tip is

$$E_z(r,\phi,t) = A(t)r^{\nu}\sin\nu\phi \tag{31}$$

$$H_x(r,\phi,t) = B(t)r^{\nu-1}\cos(1-\nu)\phi \tag{32}$$

$$H_y(r,\phi,t) = C(t)r^{\nu-1}\sin(1-\nu)\phi \tag{33}$$

where (r, ϕ) are the polar coordinates with origin at the tip of the wedge, α is the angle of the wedge, and

$$\nu = \frac{\pi}{2\pi - \alpha} \tag{34}$$

Notice that H_x and H_y are singular for $\alpha < \pi$. This singular behavior makes questionable the use of smooth interpolation functions over magnetic elements that are close to the edge for the computation of E_z at the electric nodes inside these elements. (See, for example, nodes E_1 and E_2 in Fig. 6.) In order to check this, three different approaches were taken. In the first approach, the isoparametric interpolation functions were used for the computation of the spatial derivatives of the magnetic fields, neglecting their singular behavior. The second approach was based on (31). For example, the value of the electric field at node E_3 was used in order to update the field at node E_2 through the formula

$$E_2 = E_3 \left(\frac{r_3}{r_2}\right)^{\nu} \frac{\sin \nu\phi_3}{\sin \nu\phi_2} \tag{35}$$

The value at node E_3 was found normally from the finite-element algorithm, since the magnetic element that contains the node is away from the edge and no singularities are present. The third and last approach was to use the exact results by Keller and Blank [41] for the electromagnetic scattering of pulses by perfectly conducting wedges.

The above approaches were used to solve the problem of scattering by a perfectly conducting semi-infinite plane. The geometry is shown in the insert of Fig. 7a. The incident pulse is a Gaussian with effective spatial width $15h$ and of amplitude $1V/m$. The early-time electric field for points A and B is shown in Fig. 7a and Fig. 7b, respectively. We notice that away from the wedge all three approaches give essentially the same result. On the other hand, for the point close to the tip of the wedge, the incorporation of the singularity increased the speed of convergence giving a better early time result.

The TE-case is considered next. Note that the magnetic field has only one component polarized along the axis of the wedge, while the electric field has both E_x and E_y components. The behavior of the field components at the vicinity of the edge is [35]

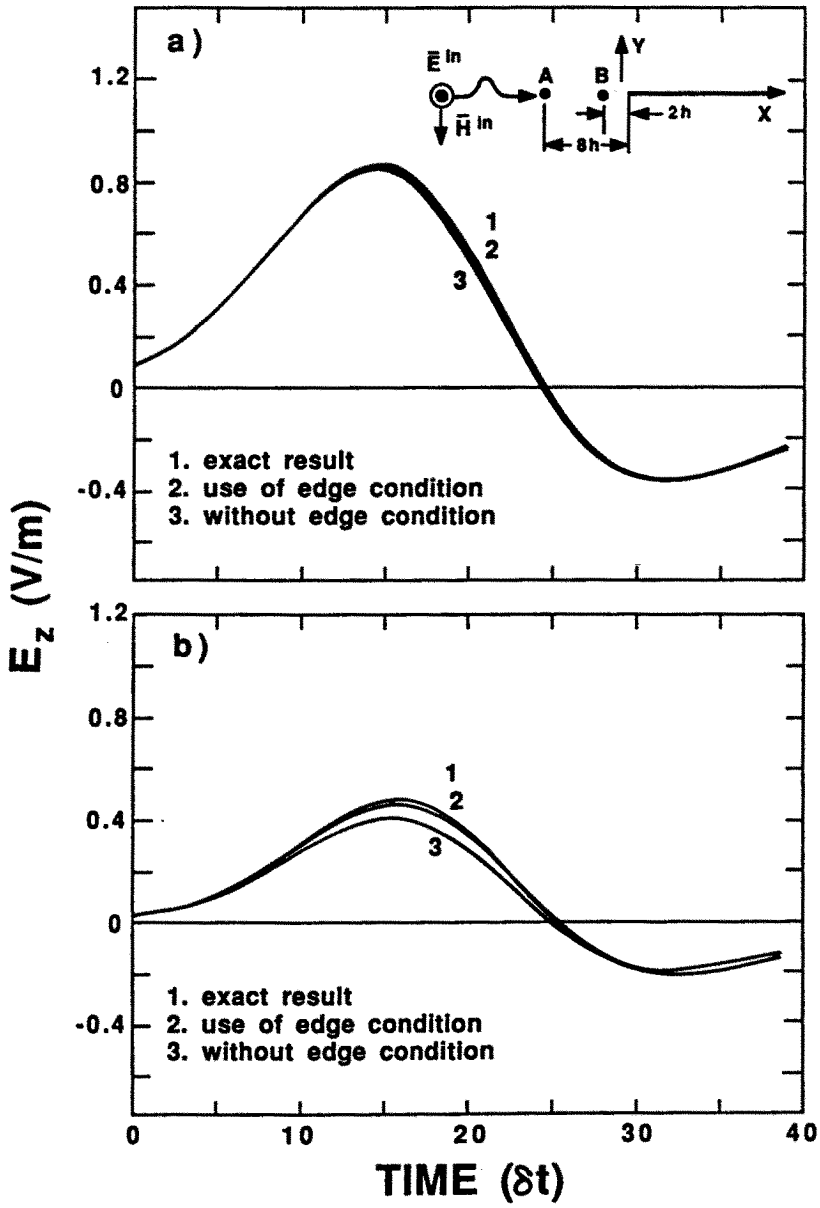

Figure 7 TM-scattering by a perfectly conducting semi-infinite plane.

$$H_z(r,\phi,t) = A_1(t) + A_2(t)r^{\nu}\cos\nu\phi \tag{36}$$

$$E_x(r,\phi,t) = B(t)r^{\nu-1}\sin(1-\nu)\phi \tag{37}$$

$$E_y(r,\phi,t) = C(t)r^{\nu-1}\cos(1-\nu)\phi \tag{38}$$

where ν is given by (34). Notice that for $\alpha < \pi$ both E_x and E_y become infinite at the edge. Two different approaches were used for the numerical simulation of the problem and were compared with the exact result of [41]. In the first approach, the singular behavior of the electric field was neglected and the leap-frog scheme was used. Only a slight modification was introduced for the computation of the electric field at the node that lies on the edge. In order to understand the motivation for this modification, let us examine (37) and (38) more carefully. First of all, it is obvious that by trying to calculate *some* value for the electric field at the tip we consciously introduce some error, since from (37) and (38) E_x and E_y are infinite there. However, we already decided that we shall neglect this singularity at the moment and we shall assume that E_x and E_y have some specific value. From (37), it is also obvious that as $r \to 0$, $E_x = 0$ on the plane $\phi = 0$, and $E_x = B(t)r^{\nu-1}\sin(\pi-\alpha) \neq 0$ on the plane $\phi = 2\pi - \alpha$. That is, even if we assume that E_x never becomes infinite, we must account for its discontinuity as $r \to 0$, since it may affect the stability of the numerical scheme [42]. An ingenious way to take care of such discontinuities in the solution of hyperbolic systems was introduced by Lax [43]. His scheme replaces the explicit approximation of the time derivative of the field at node i

$$\frac{\partial E}{\partial t} \approx \frac{E_i^{n+1} - E_i^n}{\delta t}$$

by

$$\frac{\partial E}{\partial t} \approx \frac{1}{\delta t}\left[E_i^{n+1} - \frac{1}{2}\left(E_{i+1}^n + E_{i-1}^n\right)\right] \tag{39}$$

One can easily show that the last approximation introduces an *artificial diffusion* term into the discretized equation which helps the stability of the numerical scheme. Using this technique, the following discrete

equations are used for the computation of the electric field at the node at the tip (see Fig. 6)

$$\frac{1}{\delta t}\left[E_{0x}^{n+1} - \frac{1}{2}\left(E_{4x}^{n} + E_{8x}^{n}\right)\right] = \frac{1}{\epsilon_0}\frac{H_1^{n+\frac{1}{2}} - H_4^{n+\frac{1}{2}}}{h} \tag{40}$$

$$\frac{1}{\delta t}\left[E_{0y}^{n+1} - \frac{1}{2}\left(E_{2y}^{n} + E_{6y}^{n}\right)\right] = -\frac{1}{\epsilon_0}\frac{H_2^{n+\frac{1}{2}} - H_1^{n+\frac{1}{2}}}{h} \tag{41}$$

The second approach avoids the computation of the electric field at the node at the tip, and makes use of the known behavior of the magnetic field in order to compute the values of the magnetic nodes around the edge. More specifically, for the geometry shown in Fig. 6, the magnetic field at nodes H_1, H_2, and H_4 cannot be found using the numerical algorithm since the electric field at E_0 is not known. Using the known values of the magnetic field at nodes H_3 and H_5, the coefficients A_1 and A_2 in (36) can be specified. Equation (36) is then used to compute H_z at H_1, H_2, and H_4.

The above schemes were tested and compared with the exact solution for the problem of TE-scattering by a square wedge. The geometry configuration is shown in the insert of Fig. 8a. The results for the magnetic field at points A and B are shown in Figs. 8a and 8b, respectively. We notice that for the point B close to the edge, the incorporation of the known behavior of the field gives a better result for the early-time response. The same is true for the early-time response at point A, but we notice that for later times both numerical schemes give essentially the same result as the exact solution. It is interesting to notice the effect of the artificial diffusion term which was used for the computation of curve 3. Its use gives an $\approx 8\%$ error at the peak value of the field. Experimenting with three-dimensional geometries that feature sharp corners or conical tips, we found that the use of the artificial diffusion term results in incorrect values for the fields at the vicinity of the corner. To cure this, a simple algorithm was introduced [44] which accounts for the singular behavior of the fields. The results in [44] demonstrate that in the scattering problem the differences between the use of the diffusion term and the incorporation of the singularity of the fields are limited to the region very close to the corner. The reason the error does not propagate is that the corner field, despite its singularity, only contains small part of the incident power, and eventually is covered up by fields scattered from other parts of the body.

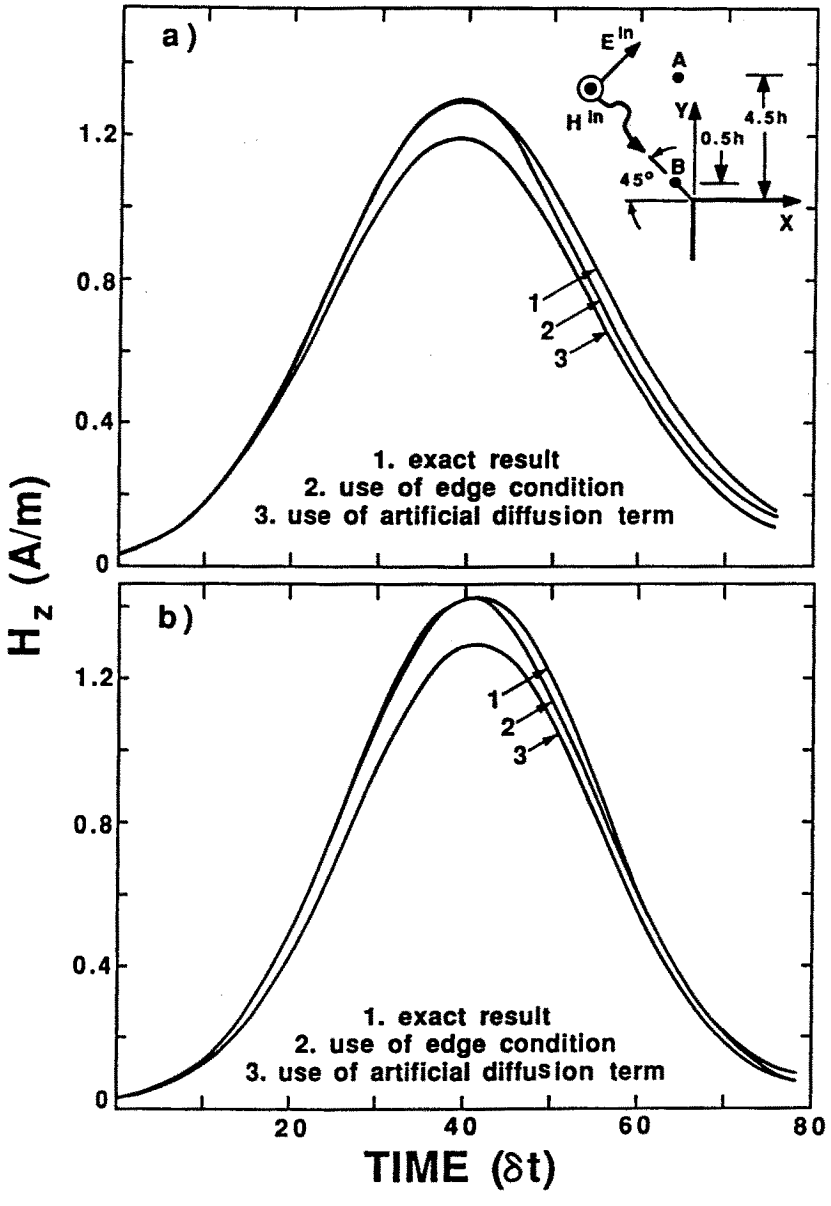

Figure 8 TE-scattering by a perfectly conducting square wedge.

This suggests that in the computation of the far-field the simple diffusion algorithm is quite adequate, assuming that no interfering obstacles (such as slots) exist in the vicinity of a corner or a wedge.

7.6 Numerical Results

The simplicity and the flexibility of the method of the conforming boundary elements allows us to study the scattering characteristics of a wide variety of scatterers. The solution of the finite-element problem gives the electric and magnetic fields everywhere on the computational grid. Probably the most useful result for the problem of scattering by perfect conductors is the induced current on their surface. Once this is found as a function of time well-known formulas can be used for the far-field computation [1]. Nevertheless, near-field information is also useful in many cases, especially in problems involving electromagnetic coupling effects, antennas on conducting structures, design of lenses, etc. One can also argue that under the assumption that the truncation boundary is set far away from the scatterer, the shape of the scattered pulse there resembles quite accurately the far-field. Our numerical simulation results showed that this was indeed the case. We actually found that the limit for r_{far} set by (28) was rather conservative. Using the fact that the lower bound for the wavelengths of the propagating waves on the grid is approximately $\lambda_{min} = 8h$ as discussed in section 7.2, (28) gives for a scatterer of $d_{max} = 20h$, $r_{far} \geq 100h$. Our results for a circular cylinder of diameter $20h$ showed that the scattered pulse had reached its far-field state at distances of about $40h$. Experimenting with different geometries and different polarizations of the incident field, we found that computed scattered fields can be assumed to have reached their far-field state for distances r such that

$$2d_{max} < r_{far} < \frac{d_{max}^2}{\lambda_{min}} \tag{42}$$

where it is assumed that $d_{max} > 2\lambda_{min}$. The lower limit $2d_{max}$ was found appropriate for two-dimensional geometries, while three-dimensional geometries seem to push r_{far} to the upper limit of (42), possibly due to the resonances associated with the finite dimensions of the scatterer.

In [18] the simple case of a circular cylinder illuminated by a plane wave pulse for both TE- and TM-polarizations was considered in order to compare the performance of the method with the one of the time-

domain integral equation [45]. A very good agreement was found for both polarizations with 3%-5% differences in the peak values. Here, the scattering from geometries with wedges and corners, as well as the propagation through lens-like media is investigated. For such problems, the solution through a time-domain integral equation formulation becomes rather involved [47].

First, the TM-scattering by a perfectly conducting cylinder with attached fins is computed. The incident pulse is a Gaussian,

$$g(t) = \exp(-\frac{(t-t_0)^2}{T^2}) \tag{43}$$

with the parameters t_0, T chosen in such a way that its spatial width is approximately equal to the diameter of the scatterer. The discretization parameters were, $h = 0.1$ m and $\delta t = 0.7h/c$. The response for broadside incidence (wave vector along $\phi = 0°$) is shown in Fig. 9 for a distance $r_{far} = 2d_{max}$. Looking at the response in the backscatter direction, we see two positive peaks, the first due to specular reflection from the front side of the cylinder, and the second due to reflection from the fins. There is also a negative swing. As a matter of fact, this negative swing is predicted by the physical optics approximation [45], even (erroneously) for a cylinder without fins. Since the physical optics approximation becomes better as the relative size of the scatterer's flat region increases, it is quite reasonable that its results for the cylinder with attached fins are more accurate than those for a plain cylinder. In Fig. 10 the TM-scattering for end-on incidence (wave vector along $\phi = 90°$) is shown. Notice the shorting effect of the fin in the backscattered field. By the time-domain reciprocity theorem [46], the scattered field should be the same if the direction of the incident and scattered fields are interchanged. Indeed, the field scattered in the direction of the plane of the fin for broadside incidence in Fig. 9 is the same with the field scattered off the circular side with end-on incidence in Fig. 10. Results for a variety of two-dimensional structures can be found in [27].

As far as three-dimensional geometries are concerned, one can, in principle, apply the method of conforming boundary elements in a very straightforward manner once the numerical mesh has been generated. Even though the automated generation of conforming three-dimensional boundary elements can be quite complicated, there are two large classes of three-dimensional scatterers that can be solved in a very simple manner. The first class includes bodies of revolution un-

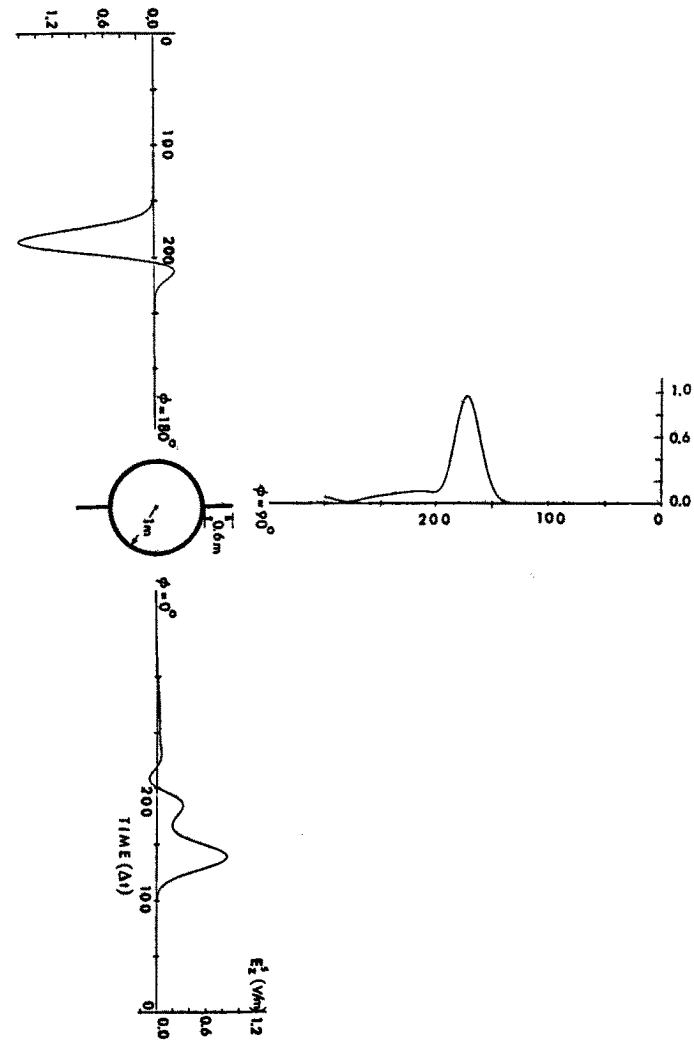

Figure 9 TM-scattering by a perfectly conducting cylinder with attached fins (broadside incidence).

der the assumption of azimuthal excitation. Such a problem is readily solved as a two-dimensional one. The second class consists of bodies generated by finite portions of infinite cylindrical structures of arbitrary cross-sections. The finite-element mesh for such structures can be generated by stacking two-dimensional grids along the axis of the

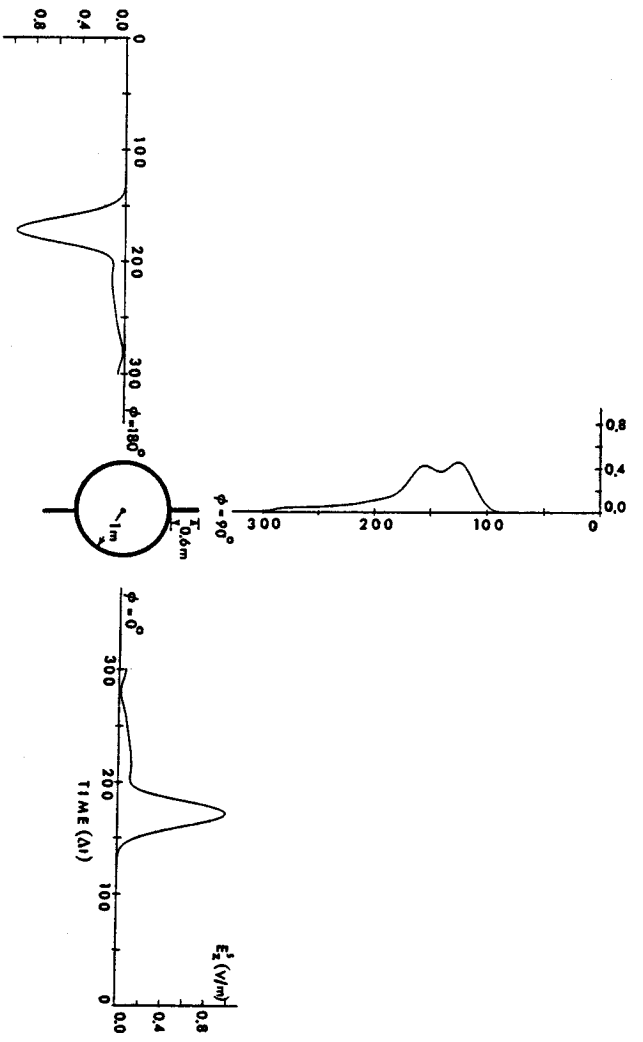

Figure 10 TM-scattering by a perfectly conducting cylinder with attached fins (end-on incidence).

structure. Such scatterers can become more complex by attaching fins to them.

Here, we present results for scattering by a cross formed by an electrically thick cylinder and a flat plate. The geometry is shown in Fig. 11. Experimental results for the induced electric charge and cur-

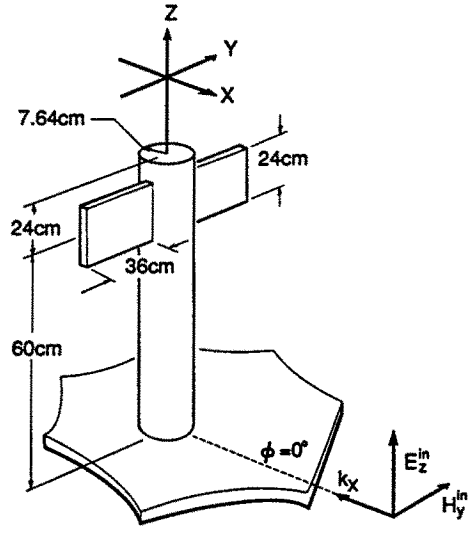

Figure 11 Conducting cylinder with attached fins.

rent densities for the geometry under consideration were available [48] and allowed us to evaluate our numerical computations. The incident field was a plane-wave sinusoidal with $\lambda = 48$ cm. For this excitation, the cylinder of Fig. 11 is a wavelength in circumference and 1.75λ high above the ground plane. Each of the arms of the flat plate is 0.75λ long, 0.2125λ wide and 0.0255λ thick. The plate is centered at a height of 1.25λ from the ground plane. The source used for the experiment was a dipole inside a corner reflector at a distance 7.5λ from the axis of the cylinder. Hence, the incident wave in the measurements was a spherical wave instead of plane one as it was assumed in the numerical simulation. The grid size h was chosen to be half the radius of the cylinder and the flat plates were assumed to have zero thickness. The computational mesh used was $(60h) \times (30h) \times (50h)$. Figure 12 illustrates the magnitude and the relative phase of the induced current density J_z along the flat plate at about 2 cm off the lower edge. The solid lines are the experimental results while the dots show the computed ones. We notice a very good agreement. An extensive presentation of the results and the comparison between theory and experiment is being prepared for publication [49].

The next example considers radiation from a slot on an infinite perfectly conducting plane. The infinite conducting plane coincides

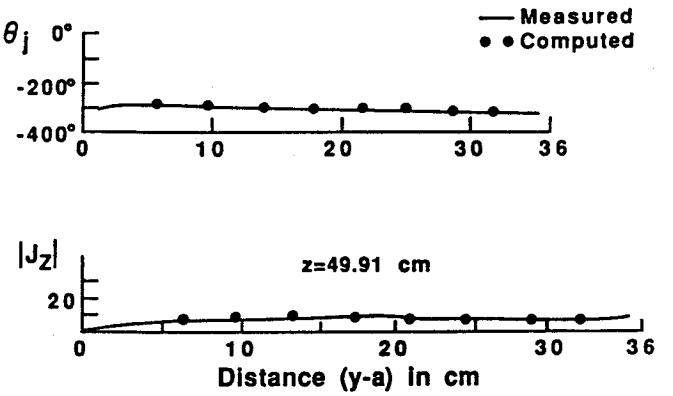

Figure 12 Induced current density J_z (amplitude and phase) along the fin.

with the xy-plane of the coordinate system and the slot is along the x-axis with its center coinciding with the origin. The length of the slot is 0.25 m and it is fed at its center by a voltage source. The excitation is a step voltage which is not abrupt, but it rises to its final constant value in the sense of a gaussian curve terminated at its peak, and from then on maintaining its peak value. The time step used in the computation was $\delta t = 0.79$ ps and the effective rise time of the step was $21(\delta t) = 16.59$ ps. The radiated electric field on the xz-plane for different angles and at a distance of 0.5 m from the origin is shown in Fig. 13. By Fourier transforming the transient response, we can compare our results with the exact frequency-domain results for radiation from a half-wavelength slot [50]. The specific slot is half-wavelength long at f=600 MHz. The comparison between our numerical solution and theory is shown in Fig. 14. It is worth mentioning that the theoretical result is for the far-field normalized to the computed value at 90°, while our numerical result is for a distance of one wavelength away from the origin. Therefore, we expect that the effect of the near-field will be present in our result and this should justify the little discrepancy from the theoretical solution. The next step was to position a hemispherical Maxwell's fish-eye lens [35] in front of the slot. The center of the hemispherical lens is on the z-axis, 0.75 m away from the origin, and its radius is $a = 0.75$ m. The relative dielectric permittivity of the lens

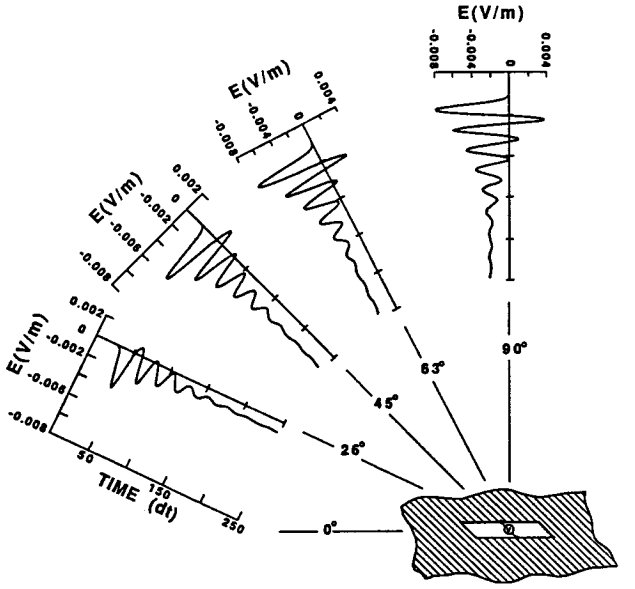

Figure 13 Transient radiation from a slot on an infinite ground plane.

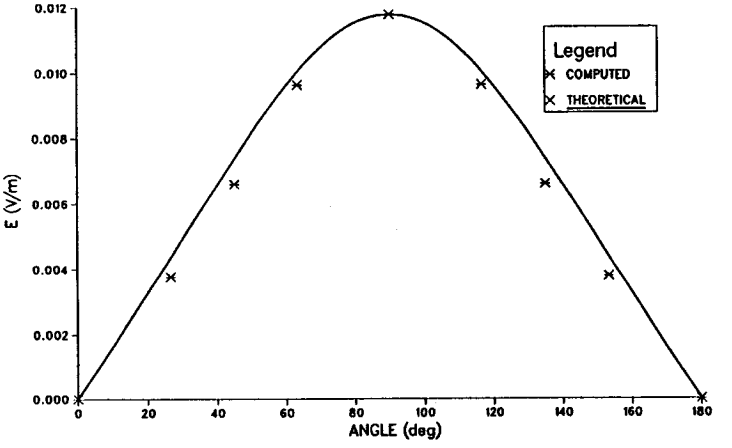

Figure 14 Radiation pattern at f=600 MHz (half-wavelength slot).

$$\epsilon_r = \frac{4}{\left[1 + \left(\frac{r}{a}\right)^2\right]^2}$$

varies nonlinearly with radius from four at the center of the hemisphere to one at $r = a$, and helps the focusing of the energy radiated by a

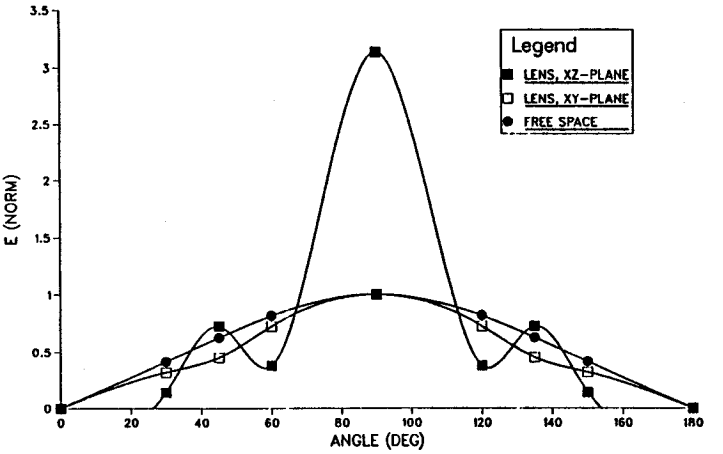

Figure 15 Radiation patterns (xz-plane, xy-plane) at f=600 MHz in the presence of a fish-eye lens.

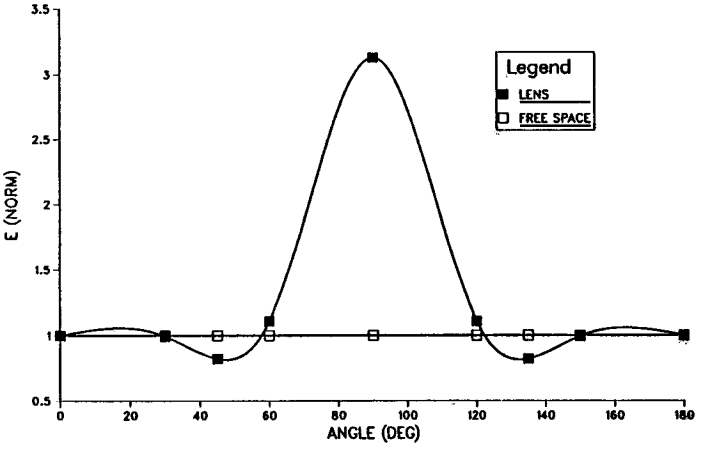

Figure 16 The yz-plane radiation pattern at f=600 MHz in the presence of a fish-eye lens.

point source at the focus. Figure 15 demonstrates this focusing effect comparing the radiation patterns for f=600 MHz. Notice that the peak of the beam at 90° on the xz-plane is about 9.9 dB above the one that occurs when the slot radiates in free-space. Finally, Fig. 16 demonstrates the fact that the radiation pattern on the yz-plane is not isotropic anymore. In conclusion, Figs. 15 and 16 make clear that the

presence of the lens improved significantly the directivity of the slot in the direction of the z-axis.

7.7 Discussion

One of the special features in the method of conforming boundary elements is that instead of generating the appropriate finite-element mesh, boundary elements are introduced close to the surface of the scatterer by combining the elements of a uniform rectangular grid with line segments that approximate the geometry of interest. Therefore, only the coordinates of these boundary elements need to be stored at the expense of a more sophisticated software for the construction of these elements. This, of course, results in big savings in computer memory, hence making possible the solution of complex problems which cannot be handled efficiently by the traditional frequency-domain techniques or the time-dependent integral equation approaches. The direct results of the numerical solution are the electric and magnetic field everywhere on the mesh at discrete time instants.

The numerical integration implements a simple explicit scheme, hence avoiding any matrix inversion. Various types of numerical errors associated with the discretization of Maxwell's equations have been discussed. The need for additional numerical conditions for the computation of the scattered fields on the truncation boundary was demonstrated and an approximate first-order radiation condition was discussed. Relations between the size of the scatterer, the characteristics of the exciting pulse, and the distance of the radiation boundary from the scatterer were given for minimizing the unphysical reflections from the artificial boundary. While second-order radiation boundary conditions are available that allow the truncation boundary to be brought closer to the scatterer, their implementation in the conforming boundary element algorithm is not as straightforward as in the time domain finite difference algorithm. In general, the choice of the order of the radiation condition to be used will depend on the available computer memory resources. The numerical simulation of the field singularities at the vicinity of conducting edges and corners was also examined. Finally, several applications of the proposed method to two- and three-dimensional problems in radiation and scattering were presented.

From the point of view of the computer simulation technology, the method was found to be a very powerful and programmer-friendly tool. Its efficiency is remarkable. A typical three-dimensional problem with

750,000 unknowns takes four minutes CPU time on a Cray-1 for 300 time steps. The modeling capability is excellent for two-dimensional geometries as well as three-dimensional ones that can be decomposed into cylindrical subregions of constant cross-section.

Acknowledgements

This work was sponsored by the Office of Naval Research under Contract N0014-86-K-042.

References

[1] Bennett, C. L., and W. L. Weeks, "Electromagnetic pulse response of cylindrical scatterers," *1968 International Antennas and Propagation Symposium*, Boston, Mass., September 1968.

[2] Liu, T. K., and K. K. Mei, "A time-domain integral equation solution for linear antennas and scatterers," *Radio Science*, **8**, 797–804, 1973.

[3] Miller, E. K., "Some computational aspects of transient electromagnetics," *EMP Interaction Notes*, Note 143, 1972.

[4] Miller, E. K., and J. A. Landt, "Direct time domain techniques for transient radiation and scattering from wires," *Proc. IEEE*, **68**, 1397–1423, 1980.

[5] Sarkar, T. K., "The application of the conjugate gradient method for the solution of transient scattering," *International URSI Symposium*, Santiago, Spain, 1983.

[6] Huiser, A. J. M., A. Quatropani, and H. P. Baltes, "Numerical solution of electromagnetic scattering problems. Case of perfectly conducting cylinders," *Optics*, Comm. **37**, 307–310, 1981.

[7] Tijhuis, A. G.,"Towards a stable marching-on-in-time method for two dimensional transient electromagnetic scattering problems," *International URSI Symposium*, Santiago, Spain, 1983.

[8] Yee, K. S.,"Numerical solution of initial boundary value problems involving Maxwell equations in isotropic media," *IEEE Trans. Antennas Propagat.*, **AP-14**, 302–307, 1966.

[9] Taylor, C. D., D. Lam, and T. H. Shumpert, "Electromagnetic

pulse scattering in time-varying inhomogeneous media," *IEEE Trans. Antennas Propagat.*, **AP-17**, 585–589, 1969.

[10] Merewether, D. E., "Transient currents induced on a metallic body of revolution by an electromagnetic pulse," *IEEE Trans. Elec. Comp.*, **EMC-13**, 41–44, 1971.

[11] Holland, R., L. Simpson, and K. S. Kunz, "Finite-difference analysis of EMP coupling to lossy dielectric structures," *IEEE Trans. Elec. Comp.*, **EMC-22**, 203–209, 1980.

[12] Taflove, A., and K. R. Umashankar, "A hybrid moment method/ finite-difference time-domain approach to electromagnetic coupling and aperture penetration into complex geometries," *IEEE Trans. Antennas Propagat.*, **AP-30**, 617–627, 1982.

[13] Borup, D. T., D. M. Sullivan, and O. P. Gandhi, "Comparison of the FFT conjugate gradient method and the finite-difference time-domain method for the 2-D absorption problem," *IEEE Trans. Microwave Theory Tech.*, **MTT-35**, 383–395, 1987.

[14] Taflove, A., and K. Umashankar,"The finite-difference time-domain (FD-TD) method for electromagnetic scattering and interaction problems," *Journal of Electromagnetic Waves and Applications*, **1**, 243–267, 1987.

[15] Mei, K. K., A. Cangellaris, and D. J. Angelakos, "Conformal time-domain finite-difference method," *International URSI Symposium*, Santiago, Spain, 1983.

[16] Ray, S. L., and N. K. Madsen, "Finite element analysis of electromagnetic aperture coupling problems," *North American Radio Science Meeting*, Vancouver Canada, 1985.

[17] Lin, C. C., *Numerical Modeling of Two-Dimensional Time-Domain Electromagnetic Scattering by Underground Inhomogeneities*, Ph. D. Dissertation, Dept. EECS, University of California, Berkeley, 1985.

[18] Cangellaris, A. C., C. C. Lin, and K. K. Mei, "Point-matched time-domain finite element methods for electromagnetic radiation and scattering,"*IEEE Trans. Antennas Propagat.*, **AP-35**, 1160–1173, October 1987.

[19] Ziolkowski, R. W., and N. K. Madsen, "Discretized exterior differential form approach to the numerical solution of Maxwell's equations," *APS-URSI Meeting*, Blacksburg, Virginia, 1987.

[20] Jurgens, T. G., A. Taflove, and K. R. Umashankar," Conformal FD-TD modeling of objects with smooth curved surfaces," *APS-URSI Meeting*, Blacksburg, Virginia, 1987.

[21] Stratton, J. A., *Electromagnetic Theory*, McGraw Hill, New York, 1941.

[22] Sommerfeld, A., *Partial Differential Equations in Physics*, Academic Press, New York, 1949.

[23] Abarbanel, S., and D. Gottlieb, "A note on the leap-frog scheme in two and three dimensions," *J. Comp. Phys.*, **21**, 351–355, 1976.

[24] Thompson, J. F., *Numerical Grid Generation*, Elsevier Science Pub., New York, 1982.

[25] Ergatudis, I., B. M. Irons, and O. C. Zienkiewicz, "Curved isoparametric quadrilateral elements for finite element analysis," *Int. J. Solids Struct.*, **4**, 31–42, 1968.

[26] Huebner, K. H., *The Finite Element Method for Engineers*, John Wiley and Sons, New York, 1975.

[27] Cangellaris, A. C., *Time-Domain Computation of Electromagnetic Wave Scattering by the Method of Conforming Boundary Elements*, Ph. D. Dissertation, EECS Department, University of California, Berkeley, 1985.

[28] Richtmyer, R. D., and K. W. Morton, *Difference Methods for Initial Value Problems*, John Wiley and Sons, New York, 1967.

[29] Vichnevetsky, R., and J. Bowles, *Fourier Analysis of Numerical Approximations of Hyperbolic Equations*, SIAM, Philadelphia, 1982.

[30] Majda, A., and B. Engquist, "Radiation boundary conditions for acoustic and elastic wave calculations," *Comm. Pure Appl. Math.*, **32**, 313–357, 1979.

[31] Gottlieb, D., and E. Turkel, "Boundary conditions for multistep finite difference methods for time dependent equations," *J. Comp. Phys.*, **26**, 181–196, 1978.

[32] Mur, G., "Absorbing boundary conditions for finite-difference approximation of the time-domain electromagnetic field equations," *IEEE Trans. Elec. Comp.*, **EMC-23**, 1073–1077, 1981.

[33] Ziolkowski, R. W., N. K. Madsen, and R. C. Carpenter, "Three-dimensional computer modeling of electromagnetic fields: A global lookback lattice transaction scheme," *J. Comp. Phys.*, **50**, 360–408, 1983.

[34] Friedlander, F. G., "On the radiation field of pulse solutions of the wave equation," *Proc. Royal Soc. of London*, **269**, 53–65, 1962.

[35] Van Bladel, J. A., *Electromagnetic Fields*, McGraw-Hill, New York, 1964.

[36] Collin, R. E., and F. J. Zucker, (eds.), *Antenna Theory, Part I*, McGraw-Hill, New York, 1969.

[37] Gustafsson, B., H.-O. Kreiss, and A. Sundström, "Stability theory of difference approximations for mixed initial boundary value problems II," *Math. of Comp.*, **26**, 649–686, 1975.

[38] Gustafsson, B., and H.-O. Kreiss, "Boundary conditions for time dependent problems with an artificial boundary," *J. Comp. Phys.*, **30**, 333–351, 1979.

[39] Trefethen, L. N., "Group velocity interpretation of the stability theory of Gustafsson, Kreiss and Sundström," *J. Comp. Phys.*, **49**, 199–217, 1983.

[40] Bayliss, A., and E. Turkel, "Radiation boundary conditions for wave-like equations," *Comm. Pure Appl. Math.*, **33**, 707–725, 1980.

[41] Keller, J. B., and A. Blank, "Diffraction and reflection of pulses by wedges and corners," *Comm. Pure Appl. Math.*, **4**, 75–94, 1951.

[42] Smith, G. D., *Numerical Solution of Partial Differential Equations: Finite Difference Methods*, 2nd ed., Oxford Univ. Press, 1978.

[43] Lax, P. D., "Weak solutions of non-linear hyperbolic equations and their numerical computations," *Comm. Pure Appl. Math.*, **7**, 157–193, 1954.

[44] Mei, K. K., and A. C. Cangellaris, "Applications of field singularities at wedges and corners to time domain finite difference or finite element methods of field computations," *Radio Science*, **22**, 1239–1246, 1987.

[45] Bennett, C. L., *A Technique for Computing the Approximate Electromagnetic Impulse Response of Conducting Bodies*, Ph. D. Dissertation, School of Electrical Engineering, Purdue University, 1968.

[46] Cheo, B. R., "A reciprocity theorem for electromagnetic fields with general time dependence," *IEEE Trans. Antennas Propagat.*, **AP-13**, 278–284, 1965.

[47] Bennett, C. L., A. M. Auckenthaler, and J. D. DeLorenzo, "Transient scattering by three-dimensional conducting surfaces with wires," *International APS Symposium*, Los Angeles, California, 1971.

[48] King, R. W. P., and D. J. Blejer, "Surface currents and charges on a cross formed by an electrically thick cylinder and a flat plate in a normally incident plane-wave field," *Radio Science*, **14**, 753–763, 1979.

[49] Cangellaris, A. C., K. K. Mei, and D. Giri, "Time-domain finite element computation and experimental verification of electromagnetic wave scattering by complex conducting structures," in preparation – contact authors for updated citation.

[50] Elliott, R. S., *Antenna Theory and Design*, Prentice-Hall, Inc., Englewood Cliffs, N.J., 1981.